Ultrafast Metal Electrodeposition Revealed by *in-situ* Optical Imaging and Theoretical Modeling towards Fast-charging Zn Battery Chemistry

Zhao Cai,[†[a]] Jindi Wang,[†[a]] Ziheng Lu,[†[b]] Renming Zhan,[[a]] Yangtao Ou,[[a]] Li Wang,[[c]] Mouad Dahbi,[[d]] Jones Alami,[[d]] Jun Lu,*[[e]] Khalil Amine,*[[e,f]] and Yongming Sun*[[a]]

[a] Dr. Z. Cai, J. Wang, R. Zhan, Y. Ou, Prof. Y. Sun
Wuhan National Laboratory for Optoelectronics, Huazhong University of Science and Technology, Wuhan 430074, China
E-mail: yongmingsun@hust.edu.cn
[b] Dr. Z. Lu
Department of Materials Science and Metallurgy, University of Cambridge, Cambridge CB3 0FS, United Kingdom
[c] Prof. L. Wang
Institute of Nuclear & New Energy Technology, Tsinghua University, Beijing 100084, China
[d] Prof. M. Dahbi and Prof. J. Alami,
Materials Science and Nano-Engineering Department, Mohammed VI Polytechnic University, Ben Guerir, Morocco
[e] Dr. K. Amine, Dr. J. Lu
Chemical Sciences and Engineering Division, Argonne National Laboratory, Lemont 60439, United States
E-mail: junlu@anl.gov; and amine@anl.gov
[f] Dr. K. Amine
Department of Material Science and Engineering, Stanford University, Stanford, CA 94305, USA.
† These authors contributed equally to this work

Supporting information for this article is given via a link at the end of the document.

Abstract: Metallic Zn is a preferred anode material for rechargeable aqueous batteries towards smart grid and renewable energy storage. Understanding how metal nucleates and grows at aqueous Zn anode is a critical and challenging step to achieve full reversibility of Zn battery chemistry, especially under fast-charging conditions. Here, by combining *in-situ* optical imaging and theoretical modeling, we uncover the critical parameters governing the electrodeposition stability of metallic Zn electrode, that is, the competition among crystallographic thermodynamics, kinetics, and Zn^{2+}-ion diffusion. Moreover, steady-state Zn metal plating/stripping with Coulombic efficiency above 99% is achieved at 10-100 mA cm^{-2} in a reasonably high concentration (3 M) $ZnSO_4$ electrolyte. Significantly, long-term cycling-stable Zn metal electrode is realized with a depth of discharge of 66.7% under 50 mA cm^{-2} in both Zn||Zn symmetrical cells and MnO_2||Zn full cells.

Introduction

Fast-charging/discharging capability is a critical parameter for energy storage devices applied in the field of smart grid and sustainable energy (such as tide, solar and geothermal) storage[1], where rechargeable aqueous Zinc (Zn) metal batteries are arousing increasing attention due to the advantages of cost-effectiveness, inherent safety, and eco-friendliness[2]. Nevertheless, the Zn battery chemistry gets into limited reversibility issue in aqueous electrolyte, as exemplified by the metallic Zn dendrites, low Coulombic efficiency, and then short rechargeable life, let along the unsatisfied power density and fast-charging capability, which are all relevant to the fundamental mechanisms on Zn electrodeposition reactions[3]. Unfortunately, the capability of fast electrodeposition for Zn metal electrode and the reaction mechanisms behind remain elusive, which are both essential and inevitable for the target development of high power Zn metal batteries with long lifespan.

In the pursue of high power density and long lifespan of Zn metal batteries, intensive efforts, including nanoscale materials/electrode design and electrolyte engineering, have been under way to improve the reversibility of Zn metal electrode under high current conditions[4]. However, it is still rare and challenging to investigate the electrodeposition reaction and reveal its practical possibility for high power application of Zn metal electrode. Although the correlation between current density and the morphology of Zn has been studied in the field of conventional electrodeposition, most of these works are based on three-electrode system or under excess electrolyte conditions, especially NaOH/KOH electrolyte for traditional alkaline Zn batteries[5]. For the recent years, $ZnSO_4$ electrolyte has been proposed as low-cost electrolyte with high electrochemical stability for neutral Zn batteries with improved reversibility[6]. Nevertheless, the metal electrodeposition under neutral Zn battery operation conditions, especially the two-electrode system with lean $ZnSO_4$ electrolyte, has not been studied yet. More importantly, achieving the dynamic electrodeposition reaction and real-time structure information of metallic Zn under battery operating conditions can help the researchers to understand the effects of various electrolytes and structures and to design advanced electrodes[7]. Therefore, it is highly desirable to investigate the dynamic Zn electrodeposition reaction and reveal the condition for high power application of Zn metal electrode, which heavily relies on both *in-situ* characterization technologies and theoretical analysis that can offer key information during the ongoing electrodeposition reaction processes.

In this work, we studied the ultrafast Zn metal electrodeposition reaction with *in-situ* optical visualization and theoretical modeling, and uncovered that the reversibility of Zn electrode was strongly correlated with the deposit morphology under various current densities: in a typical 1 M $ZnSO_4$ electrolyte, non-uniform deposit featured randomly stacked Zn nanosheets was observed at a low current densities of 1 mA cm^{-2}. With the increasing current density to 10 mA cm^{-2}, the

deposited Zn layer turned uniform with a closely packed structure. Under an ultrahigh current density of 100 mA cm^{-2}, serious concentration polarization led to the deposition of metal pillars with a tree sharp. Moreover, increasing the concentration of Zn^{2+} ions in electrolyte was found effective in widening the current density window for uniform electrochemical plating of metallic Zn, highly stable plating/stripping behavior with remarkable average Coulombic efficiency (CE) of > 99 % were achieved in a wide range of 10-100 mA cm^{-2} in 3 M $ZnSO_4$ electrolyte. Theoretical calculations further indicated that the deposition modes of metallic Zn at various current densities depend on the competition among the crystallographic thermodynamics, kinetics, and Zn^{2+}-ion diffusion, resulting in the deposit morphology of stacked hexagonal plates, horizontal dense granules, and vertical metal pillars, respectively. Based on upon understanding, highly reversible Zn metal electrode with a depth of discharge of 66.7% under ultrahigh current density of 50 mA cm^{-2} is achieved in both Zn||Zn symmetrical cells and MnO_2||Zn full cells. The ultrafast Zn electrodeposition chemistry in this work opens up new opportunities for designing advanced Zn anodes for high power and long lifespan aqueous batteries.

Results and Discussion

***In-situ* monitoring of Zn electrodeposition.**

To monitor the dynamic Zn electrodeposition reaction, *in-situ* OM investigation was conducted by employing a home-made transparent electrochemical cell (Figure 1a, S1, and S2). The electrochemical plating reaction of metallic Zn was firstly studied in 1 M $ZnSO_4$ electrolyte that commonly used in aqueous Zn batteries, and a set of typical visualization results were shown in Figure 1b–d. The plating of metallic Zn at such low current density (1 mA cm^{-2}) was quite non-uniform (Movie S1). The Zn deposits were black and porous under OM (Figure 1b), indicating a loose structure of the deposited Zn. SEM results revealed the mossy morphology for these Zn deposits, which consisted of randomly stacked sheets with average size of ~1 μm (Figure S3). The random stacking of these metallic Zn sheets led to a porous structure and overall large thickness of the Zn deposition layer. Continuous and uniform deposition of metallic Zn occurred under an increased applied current density of 10 mA cm^{-2} (Movie S2). Large Zn chunks with the size of ~20 μm were observed in the optical microscope image (Figure 1c). These uniform Zn chunks interconnected with each other closely, generating a dense structure with smooth surface in comparison to the loose deposits with rough surface achieved at 1 mA cm^{-2}. Also, the overall thickness of the deposits produced at 10 mA cm^{-2} was much thinner than that obtained at 1 mA cm^{-2} due to the closely stacked structure. SEM also verified the dense and compact structure of the Zn deposits (Figure S4). The electrodeposition of metallic Zn was vertical and non-uniform under the ultrahigh applied current density of 100 mA cm^{-2} (Movie S3, Figure 1d). The SEM results showed the Zn deposits were metal pillars with “thin roots” at the bottom and “thick crown” at the top (Figure S5), consisting of abundant of hexagonal plates. Such unique morphology of deposited Zn implied the result of an interplay of multi-factors including thermodynamic and kinetic parameters for electrochemical plating and Zn^{2+}-ion diffusion under ultrahigh current densities. Furthermore, the crystalline orientation for the Zn deposits achieved at different current densities was studied using high-resolution transmission electron microscope (HRTEM) combining with X-ray diffraction (XRD). The two-dimensional lattice fringes of Zn sheet deposits at 1 mA cm^{-2} showed clear (002) lattice fringes following three axes including (100), (010) and (110) by atomic-scale HRTEM analysis (Figure 1e). Moreover, it is noted that the XRD peak intensity of (002) and (101) demonstrated the Zn crystal growth along vertical and horizontal alignment, respectively (Figure 1f and S6), and thus the peak intensity ratio between the (002) and (101) (denoted as I_{002}:I_{101}) could be employed an indicator to show the crystalline orientation difference of the Zn deposits. A larger peak intensity ratio between $(002)_{Zn}$ and $(101)_{Zn}$ indicated the deposits were more (002)-dominant and plate-like. As shown in Figure 1g, the I_{002}:I_{101} decreased from 7.6 to 0.7 for the Zn deposits with the working current density increased from 1 to 100 mA cm^{-2}. In particular, the Zn crystal deposited at 1 mA cm^{-2} showed the highest I_{002}:I_{101} ratio of 7.6, in agreement with the (002) facet dominated sheet-like morphology (Figure 1b and 1e). The XRD analysis together with *in-situ* OM results indicated the controllable electrochemical plating behaviors of metallic Zn in aqueous electrolyte and metallic Zn deposition with various structures enabled by adjusting the applied current densities.

Effects of electrolyte concentration on Zn electrodeposition.

In the light of the above *in-situ* visualization and crystallographic anisotropy results, we systemically studied the morphology of metallic Zn deposits at different current densities (1–100 mA cm^{-2}) and fixed areal capacity (8.3 mAh cm^{-2}) in $ZnSO_4$ electrolytes with different concentrations (1–3 M). As demonstrated in Figure 2a, when electrochemical plating in 1 M $ZnSO_4$ electrolyte, there was a transformation for the morphology of the Zn deposits from randomly stacked sheets at 1 mA cm^{-2}, to densely packed chunky crystals at 10 mA cm^{-2}, and to non-uniform pillars at 100 mA cm^{-2}, which was in consistent with the *in-situ* OM results (Figure 1b–d). Increasing the electrolyte concentrations would reduce the ion-depletion region and promote the ion diffusion, beneficial for the formation of dense Zn deposits. It was found that the porosity of the plated Zn metal in 2 M $ZnSO_4$ electrolyte was obviously reduced in comparison to that in a 1 M one, as evidenced by the decreased thickness of Zn deposits in 2 M $ZnSO_4$ electrolyte (131 μm) compared with that in 1 M $ZnSO_4$ (237 μm, Figure 2b). With the increasing current density (i.e. 1 to 10 mA cm^{-2}), there was also a morphology transformation from sheets to chunky crystals (Figure S7), which was similar to the case in 1 M $ZnSO_4$ electrolyte. Chunky deposit is also beneficial to realize a dense structure. At 50 mA cm^{-2} in 2 M $ZnSO_4$, densely packed deposits were observed instead of non-uniform pillars obtained at 50 mA cm^{-2} in 1 M $ZnSO_4$, suggesting that the ion transport was promoted under such high current density condition because of the increased concentration of the electrolyte. Further increasing the electrolyte concentration to 3 M (near saturation state at room temperature), structure of the Zn deposits with much less porosity was realized at low current densities (1–10 mA cm^{-2}) in comparison to that in relatively diluted electrolyte (1–2 M $ZnSO_4$). The thickness of Zn deposits in 3 M $ZnSO_4$ was found to be the least (Figure 2c, 2d). At 1 mA cm^{-2}, the thickness of the plated Zn metal layer in 3M $ZnSO_4$ was 96 μm, much thinner than that in 2M and 1M $ZnSO_4$ (131 and 237 μm, respectively). There was also a morphology transformation from sheets to chunky crystals at 1–10 mA cm^{-2}

in 3 M $ZnSO_4$ (Figure S8). More importantly, at high current densities (10–100 mA cm^{-2}), Zn metal deposits formed a dense and compact film layer consisting of chunky crystals in 3 M $ZnSO_4$ electrolyte (Figure S9). It should be noted that concentrated electrolyte generally leads to high viscosity, thus resulting in low ionic conductivity. However, 3 M $ZnSO_4$ electrolyte showed no distinct difference in ionic conductivity to the 1 M one (Figure S10), which could be attributed to the high solvent/salt mole ratio of 18.5, much higher than the reported high concentration electrolyte with high viscosity (e.g. 2.6 for 1 M $Zn(TFSI)_2$ + 20 M LiTFSI electrolyte[8a] and 1.9 for 30 M $ZnCl_2$ electrolyte[8b]). Furthermore, the overall thickness of the deposit layer was ~40 μm (Figure 2d), which was the thinnest among all the Zn deposits obtained under all tested current densities with the same fixed areal capacity, suggesting the lowest porosity. To quantitatively analyze the porosity of Zn deposits at different current densities, the electrochemical surface area (ESA) reflected by the double-layer capacitance based on electrochemical impedance spectroscopy (EIS). As indicated in Figure 2e, S11, S12, and Table S1, the ESA of the Zn deposits in 1 M $ZnSO_4$ at 1 mA cm^{-2} was 6.63×10^{-6} μF cm^{-2}, 33.7 times of Zn deposits in 1 M $ZnSO_4$ at 10 mA cm^{-2} (1.95×10^{-7} μF cm^{-2}), indicating the higher porosity of the Zn nanosheet deposits. Moreover, the ESAs of the Zn deposits in 3 M $ZnSO_4$ at 50 mA cm^{-2} was found to be the smallest (7.73×10^{-8} μF cm^{-2}), suggesting the lowest porosity of these densely packed chunky crystals. In addition, the density of deposited Zn at 100 mA cm^{-2} was evaluated to be 6.95 g cm^{-3} (Figure S13), which was pretty close to 7.14g cm^{-3}, suggesting the compact Zn deposition. It should be noted that the Zn deposits with densely packed chunk morphology exhibited low accessible surface to electrolyte in comparison to other Zn deposits, thus minimizing the side reactions. Moreover, these densely packed chunky Zn crystals had low possibility for contact lost with current collector and the formation of “dead Zn” during cycling, which was beneficial for improving the reversibility of metallic Zn electrode. To evaluate the electrochemical reversibility of the Zn electrode, electrochemical plating/stripping investigation was performed on a Ti foil and the CE was calculated (Figure S14 and Movie S4). It should be noted that the Zn deposits on the Ti foils showed morphology of stacked nanosheets, chunky crystals, and pillars at 1 mA cm^{-2}, 10 mA cm^{-2}, and 100 mA cm^{-2}, respectively (Figure S15). This is in good accordance with that on Zn foils under the same deposition condition. Moreover, as demonstrated in Figure S16–S18, metallic Zn electrode showed relatively low CE (below 85%) when cycled in 1 M $ZnSO_4$ at low current densities of 1–5 mA cm^{-2} (porous deposits) and at high current densities of 50–100 mA cm^{-2} (metal pillars). By contrast, metallic Zn electrode exhibited the highest plating/stripping efficiency of 96.1 % at 10 mA cm^{-2} under the same conditions, in consist with the densely packed chunky crystal morphology as shown in Figure 1 and 2. The Coulombic efficiency of metallic Zn cycled in 3 M $ZnSO_4$ was overall higher than that in 1 M $ZnSO_4$. Notably, the Columbic efficiency reached nearly 100.0 % (99.2–99.8 %) at high current densities (10–100 mA cm^{-2}), suggesting the high electrochemical reversibility.

Mechanism of Zn metal electrodeposition.

To understand the ultrafast Zn metal electrodeposition reaction fundamentally, we studied the electrochemical plating kinetics of metallic Zn using computational analysis and identified the dominating factor that regulated the metallic Zn plating behavior under various conditions. Surface energy and electrochemical activation current density of various crystal planes were calculated for metallic Zn crystal with a space group of $P6_3/mmc$ (Figure 3a). The thermodynamically stable facets of hexagonal Zn metal were shown in Table S2, among which the {0001} facet was the most energetically favorable with the lowest surface energy (i.e. 0.021 eV/$Å^2$). The structure of deposited Zn shall be in conformity of the crystallographic thermodynamics at low current densities, leading to a favorable morphology of hexagonal plates with dominating facet of {0001} (also known as the Wulff construction). In the event of larger applied electrochemical overpotential/current densities, high-index facets with higher surface energies were activated, therefore simultaneous growth of various crystal planes took place and the deposition process became kinetics-controlled. Due to the activation of high-index facets, the metallic Zn crystals grew isotopically and the deposits were uniform, leading to a plat and dense deposition layer, which was desirable for battery application. By simply assuming the deposition overpotential led to the growth of high energy facets, we estimated the current densities that activated these high-index facets. As shown in Figure 3a, the activation current densities of these high-index facets were around 1 mA cm^{-2}. These results indicated that at low working current densities (< 1 mA cm^{-2}), the Zn deposits were favorable to form plate morphology with low-index facets, especially {0001}. When the applied current density increased to higher than the critical value (> 1 mA cm^{-2}), high-index facets could be accessed, and the deposition turned to kinetics-controlled, leading to more spherical and dense structures. However, at extremely high current densities such as 100 mA cm^{-2}, Zn^{2+}-ions in the electrolyte region close to the electrode would be exhausted quickly, resulting in a diffusion-controlled case where Sand’s model works. Therefore, the deposition process of these non-uniform metal pillars at ultrahigh current densities could be divided into two stages, the initial plating-controlled stage producing the “roots” and the following diffusion-controlled stage generating the “crown” of the deposits. On the basis of Sand’s model, the diffusion-limiting current density in a 1 M $ZnSO_4$ electrolyte was determined to be 21.9 mA cm^{-2} (Figure 3b). Interestingly, we found that the Sand’s limiting current density correlated strongly to the electrolyte concentration. With the $ZnSO_4$ concentration increased to 3 M, the limiting current density rose to larger than 50 mA cm^{-2}, suggesting that less concentration polarization and uniform deposition could be achieved in high-concentration electrolyte under high applied current densities. Taking the-above calculation modeling results together, it was concluded that the Zn metal electrodeposition reactions in mild $ZnSO_4$ electrolyte was controlled by multiple factors including crystallographic thermodynamics, kinetics, and Zn^{2+}-ion diffusion. As shown in Figure 3c, at low current densities (e.g. < 1 mA cm^{-2}, mode I), the metallic Zn deposition was controlled by the surface energetics and the crystallography-supported hexagonal plates were favored. With the increase of the applied current densities (e.g. 1–10 mA cm^{-2}, mode II), the metallic Zn plating kinetics started to play a role and high-index facets of metallic Zn grew. Zn metal deposits became dense and spherical in this scenario. Further, at ultrahigh current densities (e.g. 10–100 mA cm^{-2}, mode III), the plating process was diffusion-controlled and space charge region formed, where non-uniform metal pillar deposits

could be observed. It should be noted that the separator would affect the Zn deposition morphology in practical batteries under high current densities, since it might block the local ion diffusion. While the Zn||Zn symmetrical cells without separator showed stable cycling performance with a low overpotential of 50 mV at 10 mA cm^{-2} and 2 mAh cm^{-2} (Figure S19), the Zn||Zn symmetrical cells with a glass fiber separator showed a clear short circuit after several electrochemical cycles with an overpotential of 140 mV under the same test condition. These results suggested that the metal electrodeposition behavior in actual batteries should be more complicated due to the existence of separator, especially under high current densities, where further research is needed. However, the separator have little impact on the Zn deposition morphology under low current densities since the crystallographic thermodynamics and kinetics of Zn holds the key to determine the Zn morphology at this stage. The deposited Zn showed a nanosheet morphology in Zn||Zn symmetrical cells with a glass fiber separator at 1 mA cm^{-2} (Figure S20), which implied that the correlation between current density and the Zn morphology we established under condition of low current densities could be applicable in actual batteries. In addition, the morphology of Zn metal electrode in Zn||Zn symmetrical cells after 100 deposition/dissolution cycles at 10 mA cm^{-2} and 2 mAh cm^{-2} was also investigated using SEM. As shown in Figure S21, the Zn electrodes after the 1^{st}, 10^{th}, and 100^{th} cycle all showed a flat and dense Zn deposition layer with chunky crystal morphology, indicating the dense Zn deposition under realistic conditions. These results suggested that these electrochemical reactions could be controlled to achieve uniform Zn plating at an appropriate range of current density and electrolyte concentration, which should be beneficial to improve electrochemical reversibility of Zn metal electrode and enable high power Zn metal batteries with long cycle life.

Reversible Zn plating at high current density.

Emboldened by the high electrochemical reversibility, Zn||Zn symmetric cells with $ZnSO_4$ electrolyte were assembled and cycled at a high current density of 50 mA cm^{-2} and an areal capacity of 10 mAh cm^{-2}. To benefit the energy density of Zn batteries, a thin Zn metal electrode with thickness of ~26 μm was employed in this work (Figure S22) and a depth of discharge (DOD) of 66.7 % was achieved. To reduce the influence of mass transport in electrolyte during fast charging/discharging condition, regular glass fiber separator was replaced with a glass fiber gasket during the cell fabrication (Figure S23, S24). As shown in Figure 4a, the as-fabricated Zn||Zn symmetrical cells exhibited stable electrochemical cycling with a low overpotential (i.e. 106 mV) for over 100 cycles, which could completely vie with the best reported thin Zn metal electrodes under ultrahigh current densities and areal capacities thus far (Table S3). The electrochemical Zn plating/stripping behavior under ultrahigh current densities was further studied using Zn||Ti cells at 50 mA cm^{-2}, which displayed stable plating/stripping curves and a remarkable average CE of 99.2% for 100 cycles (Figure 4b). To get insight into the outstanding electrochemical plating/stripping behavior of metallic Zn under ultrahigh current densities, the charge transfer resistance for the Zn||Zn symmetrical cell was evaluated, which exhibited an ultralow value of 0.1 ohm (Figure 4c), suggesting ultrafast ion diffusion at the electrolyte/electrode interface. In addition, The Zn metal electrode showed a dense and uniform surface structure consisting of closely packed and hexagonal crystals after 10 plating/stripping cycles at 50 mA cm^{-2} and 10 mAh cm^{-2} (inset of Figure 4c), suggesting an ideal metal plating/stripping behavior. To investigate possibility of Zn metal electrode for high power applications, MnO_2||Zn cells were fabricated. As shown in Figure 4d and 4e, the aqueous MnO_2||Zn cell presented considerable cyclic stability with a capacity retention of 75.8 % after 100 cycles at 50 mA cm^{-2} and an outstandingly high CE of 99.97 %. Besides, the XRD and X-ray photoelectron spectroscopy (XPS) analysis of Zn anodes in MnO_2||Zn battery showed little change during cycling at 50 mA cm^{-2} (Figure S25), which was in consistent with the high CE and reversibility of Zn anode cycling under high current densities.

Conclusion

In this work, we investigated the ultrafast and reversible Zn metal electrodeposition in aqueous $ZnSO_4$ electrolyte to enable stable cycling of aqueous Zn electrode (> 100 cycles) with a DOD of 66.7 % at current density as high as 50 mA cm^{-2}. Both *in-situ* optical visualization and theoretical modeling confirmed the dynamic electrodeposition of Zn metal at different current densities: A transition for the plating behavior from thermodynamically favourable Zn plates to kinetic-controlled packed crystals, to diffusion-limited metal pillars was observed in a typical 1 M $ZnSO_4$ electrolyte with the working current density increased from 1 to 100 mA cm^{-2}. High electrolyte concentration (e.g. 3 M $ZnSO_4$) facilitated the ion diffusion and increased the Sand's limiting current density, leading to a densely packed morphology with high conformity for the deposits at high current densities (10-100 mA cm^{-2}), thus enabling high CE (> 99 %). The findings in this work shed light on the fundamental understanding of Zn metal nucleation and growth under various battery operating conditions, guiding the design of high power Zn metal batteries with long cycle life.

Acknowledgements

Prof. Y. Sun acknowledges the financial support by the Innovation Fund of Wuhan National Laboratory for Optoelectronics of Huazhong University of Science and Technology. Dr. Z. Cai thanks the China Postdoctoral Science Foundation (No. 2018M640694, 2020T130223). The authors would like to thank the Analytical and Testing Center of Huazhong University of Science and Technology as well as the Center for Nanoscale Characterization & Devices of Wuhan National Laboratory for Optoelectronics for providing the facilities to conduct the characterization. Work at Argonne National Laboratory was supported from Clean Vehicles, US-China Clean Energy Research Centre (CERC-CVC2) under US DOE EERE Vehicle Technologies Office. Argonne National Laboratory is operated for DOE Office of Science by UChicago Argonne, LLC, under contract number DE-AC02-06CH11357.

Keywords: Aqueous battery • fast-charging • Zn anode • electrodeposition • reversibility

[1] a) Y. Liu, Y. Zhu, Y. Cui, *Nat. Energy* **2019**, *4*, 540-550; b) Y. Liang, H. Dong, D. Aurbach, Y. Yao, *Nat. Energy* **2020**, *5*, 646-656; c) R. F. Service, *Science* **2021**, *372*, 890-891; d) W. Chen, G. Li, A. Pei, Y. Li, L. Liao, H. Wang, J. Wan, Z. Liang, G. Chen, H. Zhang, J. Wang, Y. Cui, *Nat. Energy* **2018**, *3*, 428-435; e) Y. Jin, L. Zou, L. Liu, M. H. Engelhard, R. L. Patel, Z. Nie, K. S. Han, Y. Shao, C. Wang, J. Zhu, H. Pan, J. Liu, *Adv. Mater.* **2019**, *31*, 1900567; f) C. Fang, B. Lu, G. Pawar, M. Zhang, D. Cheng, S. Chen, M. Ceja, J.-M. Doux, H. Musrock, M. Cai, B. Liaw, Y. S. Meng, *Nat. Energy* **2021**, *6*, 987–994.

[2] a) J. Huang, J. Zhou, S. Liang, *Acta Phys.-Chim. Sin.* **2021**, *37*, 2005020; b) Y. An, Y. Tian, C. Liu, S. Xiong, J. Feng, Y. Qian, *ACS Nano* **2021**, *15*, 15259-15273; c) Y. Jin, K. S. Han, Y. Shao, M. L. Sushko, J. Xiao, H. Pan, J. Liu, *Adv. Funct. Mater.* **2020**, *30*, 2003932; d) M. Zhou, S. Guo, J. Li, X. Luo, Z. Liu, T. Zhang, X. Cao, M. Long, B. Lu, A. Pan, G. Fang, J. Zhou, S. Liang, *Adv. Mater.* **2021**, *33*, 2100187; e) Z. Guo, L. Fan, C. Zhao, A. Chen, N. Liu, Y. Zhang, N. Zhang, *Adv. Mater.* **2021**, *33*, 2105133; f) Q. Zhang, J. Luan, X. Huang, Q. Wang, D. Sun, Y. Tang, X. Ji, H. Wang, *Nat. Commun.* **2020**, *11*, 3961; g) D. Li, L. Cao, T. Deng, S. Liu, C. Wang, *Angew. Chem. Int. Ed.* **2021**, *60*, 13035-13041; h) Z. Cao, P. Zhuang, X. Zhang, M. Ye, J. Shen, P. M. Ajayan, *Adv. Energy Mater.* **2020**, *10*, 2001599; i) Z. Zhao, R. Wang, C. Peng, W. Chen, T. Wu, B. Hu, W. Weng, Y. Yao, J. Zeng, Z. Chen, P. Liu, Y. Liu, G. Li, J. Guo, H. Lu, Z. Guo, *Nat. Commun.* **2021**, *12*, 6606.

[3] a) X. Zeng, J. Hao, Z. Wang, J. Mao, Z. Guo, *Energy Storage Mater.* **2019**, *20*, 410-437; b) Z. Cai , Y. Ou , J. Wang , R. Xiao , L. Fu , Z. Yuan , R. Zhan , Y. Sun, *Energy Storage Mater.* **2020**, *27*, 205-211; c) Q. Yang, G. Liang, Y. Guo, Z. Liu, B. Yan, D. Wang, Z. Huang, X. Li, J. Fan, C. Zhi, *Adv. Mater.* **2019**, *31*, 1903778; d) X. Yang, C. Li, Z. Sun, S. Yang, Z. Shi, R. Huang, B. Liu, S. Li, Y. Wu, M. Wang, Y. Su, S. Dou, J. Sun, *Adv. Mater.* **2021**, *33*, 2105951; e) J. Shin, J. Lee, Y. Park, J. W. Choi, *Chem. Sci.* **2020**, *11*, 2028-2044; f) H. Qiu, X. Du, J. Zhao, Y. Wang, J. Ju, Z. Chen, Z. Hu, D. Yan, X. Zhou, G. Cui, *Nat. Commun.* **2019**, *10*, 5374.

[4] a) R. Xiao, Z. Cai, R. Zhan, J. Wang, Y. Ou, Z. Yuan, L. Wang, Z. Lu, Y. Sun. *Chem. Eng. J.* **2021**, *420*, 129642; b) Z. Wang, J. Huang, Z. Guo, X. Dong, Y. Liu, Y. Wang, Y. Xia, *Joule* **2019**, *3*, 1289-1300; c) J. Wang, Z. Cai, R. Xiao, Y. Ou, R. Zhan, Z. Yuan, Y. Sun, *ACS Appl. Mater. Interface* **2020**, *12*, 23028-23034; d) X. Guo, Z. Zhang, J. Li, N. Luo, G.-L. Chai, T. S. Miller, F. Lai, P. Shearing, D. J. L. Brett, D. Han, Z. Weng, G. He, I. P. Parkin, *ACS Energy Lett.* **2021**, *6*, 395-403; e) M. Yan, N. Dong, X. Zhao, Y. Sun, H. Pan, *ACS Energy Lett.* **2021**, *6*, 3236-3243; f) Y. Chu, S. Zhang, S. Wu, Z. Hu, G. Cui, J. Luo, *Energy Environ. Sci.* **2021**, *14*, 3609-3620; g) Z. Cai, Y. Ou, B. Zhang, J. Wang, L. Fu, M. Wan, G. Li, W. Wang, L. Wang, J. Jiang, Z. W. Seh, E. Hu, X.-Q. Yang, Y. Cui, Y. Sun, *J. Am. Chem. Soc.* **2021**, *143*, 3143-3152; h) J. Zheng, Q. Zhao, T. Tang, J. Yin, C. D. Quilty, G. D. Renderos, X. Liu, Y. Deng, L. Wang, D. C. Bock, C. Jaye, D. Zhang, E. S. Takeuchi, K. J. Takeuchi, A. C. Marschilok, L. A. Archer, *Science* **2019**, *366*, 645-648; i) L. Cao, D. Li, T. Pollard, T. Deng, B. Zhang, C. Yang, L. Chen, J. Vatamanu, E. Hu, M. J. Hourwitz, L. Ma, M. Ding, Q. Li, S. Hou, K. Gaskell, J. T. Fourkas, X.-Q. Yang, K. Xu, O. Borodin, C. Wang, *Nat. Nanotech.* **2021**, *16*, 902-910.

[5] a) K. Raeissi, A. Saatchi, M.A. Golozar, J. Appl. Electrochem. 2003, 33, 635-642; b) T. Boiadjieva, M. Monev, A. Tomandl, H. Kronberger, G. Fafilek, *J. Solid State Electr.,* **2009,** *13*, 671-677; c) D. Grier, E. Ben-Jacob, R. Clarke, L. M. Sander, Phy. Rev. Lett., 1986, 56, 1264; d) V. Yufit, F. Tariq, D. S. Eastwood, M. Biton, B. Wu, P. D. Lee, N. P. Brandon, *Joule* **2019,** *3*, 485-502.

[6] a) X. Zheng, T. Ahmad, W. Chen, *Energy Storage Mater.* **2021**, *39*, 365-394; b) M. Song, H. Tan, D. Chao, H. J. Fan, *Adv. Funct. Mater.* **2018**, *28*,1802564.

[7] a) P. Liang, J. Yi, X. Liu, K. Wu, Z. Wang, J. Cui, Y. Liu, Y. Wang, Y. Xia, J. Zhang, *Adv. Funct. Mater.* **2020**, *30*, 1908528; b) S. Wu, S. Zhang, Y. Chu, Z. Hu, J. Luo, *Adv. Funct. Mater.* **2021**, *31*, 2107397; c) Y. Zeng, X. Zhang, R. Qin, X. Liu, P. Fang, D. Zheng, Y. Tong, X. Lu, *Adv. Mater.* **2019**, *33*, 1903675; d) Y. Yin, S. Wang, Q. Zhang, Y. Song, N. Chang, Y. Pan, H. Zhang, X. Li, *Adv. Mater.* **2020**, *32*, 1906803; e) H. Yan, S. Li, Y. Nan, S. Yang, B. Li, *Adv. Energy Mater.* **2021**, *11*, 2100186; f) P. Zou, R. Zhang, L. Yao, J. Qin, K. Kisslinger, H. Zhuang, H. L. Xin, *Adv. Energy Mater.* **2021**, *11*, 2100982; g) J. Zheng, D. C. Bock, T. Tang, Q. Zhao, J. Yin, K. R. Tallman, G. Wheeler, X. Liu, Y. Deng, S. Jin, A. C. Marschilok, E. S. Takeuchi, K. J. Takeuchi, L. A. Archer, *Nat. Energy* **2021**, *6*, 398-406; h) X. Xu, Y. Chen, D. Zheng, P. Ruan, Y. Cai, X. Dai, X. Niu, C. Pei, W. Shi, W. Liu, F. Wu, Z. Pan, H. Li, X. Cao, *Small* **2021**, *17*, 2101901.

[8] a) F. Wang, O. Borodin, T. Gao, X. Fan, W. Sun, F. Han, A. Faraone, J. A Dura, K. Xu, C. Wang, *Nat. Mater.,* **2018**, *17*, 543-549; b) C. Zhang, J. Holoubek, X. Wu, A. Daniyar, L. Zhu, C. Chen, D. P. Leonard, I. A. Rodrıguez-Perez, J.-X. Jiang, C. Fang, X. Ji, *Chem. Commun.,* **2018,** *54*, 14097-14099.

Figures

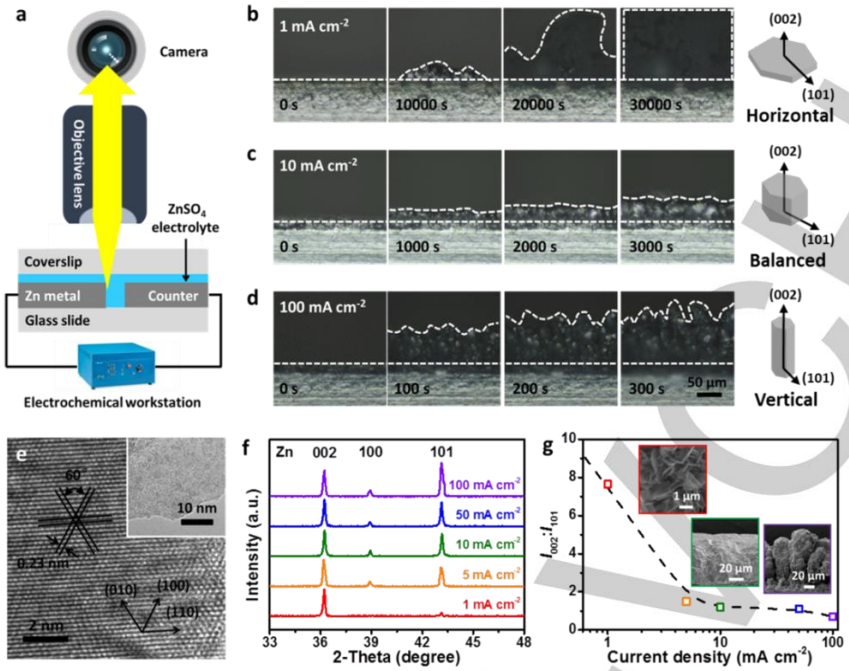

Figure 1. (a) Schematic of the transparent electrochemical cell for *in-situ* optical imaging. The Zn metal electrode was covered by water-resistant epoxy to ensure the working area at cross-section. *Operando* OM images of plated Zn metal in $ZnSO_4$ electrolyte at (b) 1 mA cm^{-2} for 30000 s, (c) 10 mA cm^{-2} for 3000 s, and (d) 100 mA cm^{-2} for 300 s. (e) HRTEM image of Zn sheet deposits at 1 mA cm^{-2}, demonstrating the atomic (002) lattice fringes. The inset showed the HRTEM image of as-deposited Zn sheet. (f) XRD patterns for the Zn metal deposited at different current densities (1–100 mA cm^{-2}). (g) Peak intensity ratio of the $(002)_{Zn}$: $(101)_{Zn}$ deduced from the XRD patterns in (f). The insets in (g) showed the SEM images of the metallic Zn deposited at 1 mA cm^{-2} (red), 10 mA cm^{-2} (green), and 100 mA cm^{-2} (purple).

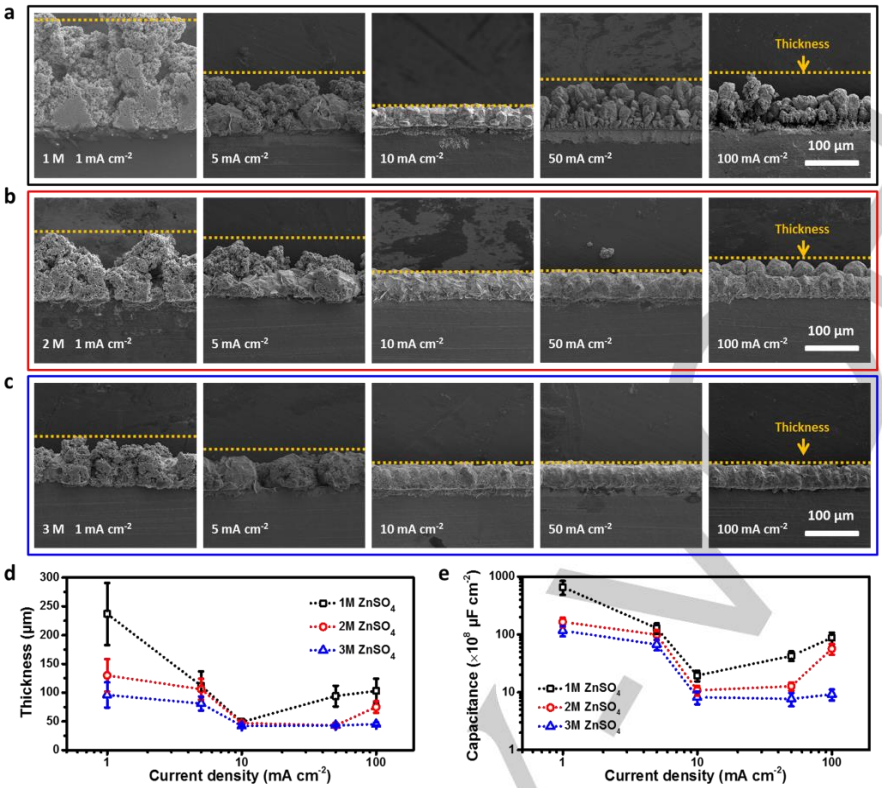

Figure 2. SEM images of the Zn metal deposited at different current densities (1–100 mA cm^{-2}) in (a) 1 M, (b) 2 M, and (c) 3 M $ZnSO_4$ electrolyte. (d) Thickness and (e) ESA reflected by the electrochemical double layer capacitance of Zn deposits at 1–100 mA cm^{-2} in 1–3M $ZnSO_4$ electrolyte.

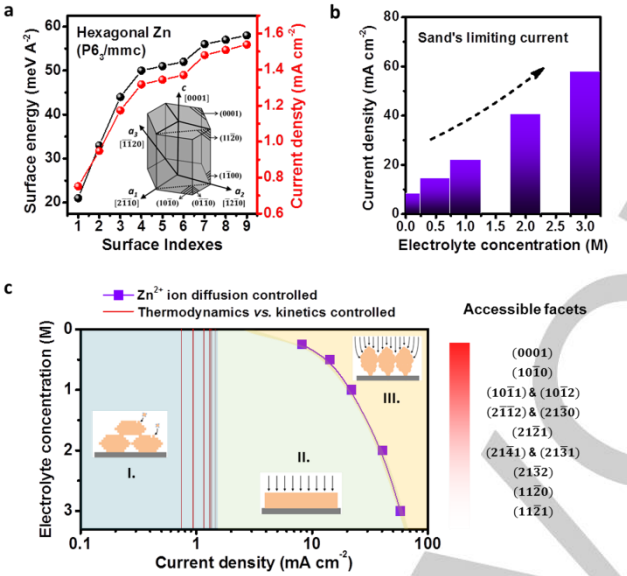

Figure 3. (a) Surface energy and electrochemical activation current density of various crystal planes of Zn metal. The inset shows the Wulff construction of hexagonal Zn metal crystal; (b) Sand's limiting current densities for Zn electrodeposition in $ZnSO_4$ electrolyte with different concentrations; (c) Illustration of different morphology evolution modes of Zn deposits governed by the crystallographic thermodynamics, kinetics and Zn^{2+}-ion diffusion at different current densities and electrolyte concentrations, indicating that mode II is good for improving the reversibility of Zn metal electrode.

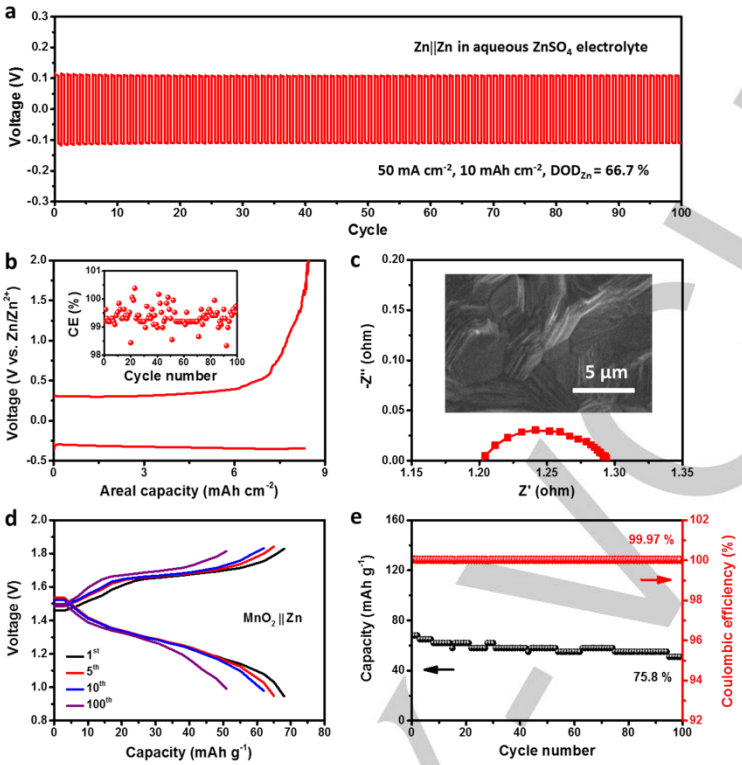

Figure 4. (a) Voltage profile of Zn||Zn symmetric cell with a glass fiber gasket at 50 mA cm^{-2} and 10 mAh cm^{-2}. (b) Voltage-areal capacity plot of Zn||Ti cell at 50 mA cm^{-2} in $ZnSO_4$ electrolyte for the 100^{th} cycle. The inset shows the Coulombic efficiency-cycle number pots for 100 cycles. (c) EIS results of Zn||Zn symmetric cell after 10 electrochemical cycles at 50 mA cm^{-2} and 10 mAh cm^{-2}. The inset shows a SEM image of Zn metal electrode after 10 cycles, displaying a dense and uniform surface. (d) Charge/discharge curves and (e) cyclic stability of Zn||MnO_2 full cells employing glass fiber gasket at 50 mA cm^{-2}.

Entry for the Table of Contents

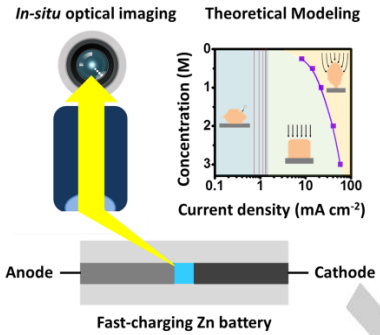

Ultrafast metal electrodeposition in fast-charging Zn batteries was investigated by *in-situ* optical imaging and theoretical modeling. The critical parameters governing the electrodeposition stability of metallic Zn electrode were uncovered, guided by which a highly reversible Zn metal electrode in aqueous battery with a depth of discharge of 66.7 % at 50 mA cm^{-2} was achieved.